Exchange bias and inhomogeneous spin states in La$_{1.5}$Sm$_{0.5}$NiMnO$_6$

R. Hissariya [ORCID],[*] N. Tripathi, and S. K. Mishra [ORCID][†]

School of Materials Science and Technology, Indian Institute of Technology (BHU), Varanasi-221005, India

Vivekanand Shukla[‡]

Chair of Theoretical Chemistry, Technische Universität Dresden, Bergstraße 66, 01069 Dresden, Germany
and Computational materials Physics Laboratory, Department of Physics, Indian Institute of Technology Ropar, 140001- Punjab, India

T. Brumme [ORCID][§]

Chair of Theoretical Chemistry, Technische Universität Dresden, Bergstraße 66, 01069 Dresden, Germany

The presence of antisite disorder in double perovskites manifests various intriguing properties like the spin-glass state, exchange bias, and memory effect. Here, we report the synthesis of a La$_{1.5}$Sm$_{0.5}$NiMnO$_6$ compound that crystallizes in a monoclinic ($P2_1/n$) structure. The presence of multiple oxidation states of Ni(Mn) cations induces competing (ferromagnetic and antiferromagnetic) exchange interactions that originate an inhomogeneous spin state, as evident from observed magnetic anomalies in temperature-dependent magnetization measurements. A spin-glass (SG) state is evolved that manifests field cooling ($H_{CF} = 500$ Oe) induced exchange bias ($H_{EB} \sim 153$ Oe) below spin-glass temperature T_{SG} (65 ± 1 K). The strength of the exchange bias is reduced after successive magnetization reversal cycles performed at 5 K. The reported magnetic training effect is explained within the frameworks of metastable magnetic disorder across frozen antiphase boundaries in the frustrated SG state. Measurements of frequency-dependent ac-susceptibility $\chi(\omega)$ suggest critical slowing dynamics and memory effect in the proximity of T_{SG}, which is described using a critical slowing model resulting in relaxation exponent z$v = 1.99 \pm 0.04$ and $\tau_0 = 8.91$ x 10^{-7}s. Employing first-principles calculations, we find the insulating ferromagnetic ground state of La$_{1.5}$Sm$_{0.5}$NiMnO$_6$ in the ordered phase where Ni(Mn) appears to be in the 2+(4+) state. Further, the presence of antisite disorder eventually results in lower magnetic moments per formula unit, which is well corroborated by experimental observations. Our findings provide a pathway for designing host materials with inhomogeneous spin-frustrated systems and variable electronic states.

I. INTRODUCTION

Uncompensated spin across the antiphase boundary (APB) that controls the exchange bias (EB) phenomenon in heterogeneous magnetic systems is considered an interesting topic in condensed matter [1–4]. The underlying ferromagnetic (FM) and antiferromagnetic (AFM) exchange interactions in the spin-glass (SG) system show local spin frustration and magnetic disorder, facilitating the microscopic mechanism for the EB phenomena and critical slowing dynamics [5–7]. The antisite disorder (ASD) mediates competition between FM and AFM exchange interactions and spin frustration that is essential in stabilizing a magnetic heterogeneous SG phase [8–11]. Studying the ordered to disordered SG phase transition and its dynamics remain crucial for various magnetic systems [8–11]. In the presence of external stimuli such as magnetic field and cooling (heating) thermal cycles, the SG phase of these frustrated systems exhibits behavior magne-

tization relaxation and memory effects [2–11]. The degree of pinned phase boundaries across the SG phase determines the mechanism of the EB effect [5,10–15]. The emergence of the SG phase has been manifested across the vast varieties of materials, such as diluted magnetic alloys [6–8], spinel [16], pyrochlore [11], garnets [12], perovskites [13,14,17], and magnetic heterostructures [2,5,18]. Moreover, several numerical models have been proposed to describe the SG state in these systems that show their impact in various fields ranging from neural networks to condensed matter [8,9,19].

The strongly correlated double perovskites ($A_2BB'O_6$; A: rare earth, B/B': transition metals) manifest competing FM and AFM exchange interactions that induce a magnetic frustrated SG state and coupling between lattice, orbital, and spin degrees of freedoms [15,20–29]. Multiple studies have been performed to investigate the role of ASD and APB on the underlying SG state of double perovskites [23,24,30–33]. For example, Sahoo *et al.* [24] reported a SG phase and memory effect in LaSrCoFeO$_6$. The La$_{2-x}$Sr$_x$NiMnO$_6$ compound manifests a variable exchange bias field and SG state [30–32]. The presence of ASD in these compounds has also been examined through the various magnetic characterizations [34–36]. The coexistence of ordered and disordered sites results in competing exchange interactions, magnetic frustration, and reduced saturation

---

*Contact author: ramanhissariya.rs.mst18@iitbhu.ac.in; Present address: Indian Institute of Technology, Bombay.

[†]Contact author: shrawan.mst@iitbhu.ac.in

[‡]Contact author: vivekanand.shukla@iitrpr.ac.in

[§]Contact author: thomas.brumme@tu-dresden.de

magnetization [23,24,30–32,37]. Wang *et al.* [38] proposed that by changing the growth procedure of systems, the degree of ASD in the lattice can be changed. Murthy *et al.* [31] reported coupling between exchange interactions and ASD for a $La_{2-x}Sr_xCoMnO_6$ compound. Pronounced structural distortion indicates competitive magnetic interactions between short-range FM and long-range AFM interactions. ASD breaks the FM ordering and drives the system toward the SG state. First-principles DFT calculations predicted that the ASD increases with Sr substitution at the La site in La_2CoMnO_6 [39]. For a spin-frustrated system, the interfacial anisotropy across FM and AFM phases boundaries induces the EB effect, which is referred to as a horizontal deviation of the magnetic hysteresis loop shifted away from the central position [2–5].

$SmNiO_3$ [40] exhibits a metal-insulator transition above room temperature that is applicable to advanced electronics and optoelectronics [41]. Electronic reconstruction at the $LaNiO_3/LaMnO_3$ interface shows charge and orbital reconstruction, charge-transfer, and intriguing magnetic properties [42,43]. These exceptional magnetic properties of $LaNiO_3/LaMnO_3$ interfaces and the renewed interest in $SmNiO_3$ perovskite are the main motivations to synthesize and study the structural and magnetic properties of $La_{1.5}Sm_{0.5}NiMnO_6$. Most previous studies have emphasized the hole doping, mainly Sr^{2+} (Ca^{2+}) at La sites or those ions with $6s^2$ lone pair electrons Bi^{3+}, (Pb^{2+}) to enable a strong interaction to the coordinated O-2p electrons and induce noncentrosymmetric domains via local substantial lattice distortion [24,31,44]. The present paper focuses on electron doping using Sm^{3+} instead of La^{3+}, which introduces the strong influence of rare-earth magnetic moment ordering at lower temperatures. The model of $La_{1.5}Sm_{0.5}NiMnO_6$ was constructed by replacing fourth of either half of $LaNi_{0.5}Mn_{0.5}O_3$ in La_2NiMnO_6 with Sm^{3+}, taking into account the order (disorder) ratio of 0.5 and the full crystal structural optimization. The present paper provides the details of the occurrence of ASD and its effects on the magnetic properties of the SG state. The field-dependent magnetic isotherm loops display a notable EB effect described in terms of disordered pinning centers and frozen spins in this inhomogeneous system. Simultaneously, spin freezing dynamics, memory effect, and magnetic training effect are presented. An interesting observation of the transformation of the conventional SG state of the parent La_2NiMnO_6 compound into a cluster spin-glass state in $La_{1.5}Sm_{0.5}NiMnO_6$ (LSNMO) is detected, highlighting a core issue of condensed matter related to spin-freezing and jamming spin dynamics.

II. MATERIALS AND METHODS

A. Experimental methods

The polycrystalline LSNMO compound was prepared through the *sol-gel* route using high-purity aqueous precursors [21,38,45]. The proportionate ratio of pure $La(NO_3)_3.6H_2O$, $Sm(NO_3)_3.6H_2O$, $Ni(NO_3)_2.6H_2O$, and $C_4H_6MnO_4.4H_2O$ were dissolved in 2-methoxy ethanol and mixed until the solution turned transparent. The cationic solutions were stirred for 2 h to prepare the sol, which was cured at 340 K for 12 h to obtain the gel. Finally, the gel was dried at 470 K to extract the powder calcined at 1050 K for 5 h to get the pure

phase of the LSNMO compound. The structural details and phase purity of the polycrystalline powders were examined by an x-rays diffraction (XRD) (Rigaku, Tokyo, Japan) method using a Cu-K_α ($\lambda = 1.5406$ Å) as a radiation source at room temperature. The XRD pattern was recorded across 20–90° at the scan rate of 2°/min. The electronic state of Mn and Ni elements was determined by x-ray photoemiission spectroscopy (XPS, Thermo Fisher Scientific) at room temperature. The electronic structure of Mn and Ni were also verified with x-ray absorption spectroscopy (not shown) that matched with XPS findings. Magnetization measurements were performed with a magnetometer (SQUID, Quantum Design, USA) under zero-field-cooled (ZFC) and field-cooled (FC) conditions across a 300–5 K temperature range under an applied magnetic field of 100 and 500 Oe. The ZFC/FC measurements were recorded during the warming mode with the following steps: (i) the sample was first cooled without any external magnetic field from 300 K → 5 K, (ii) at 5 K, a constant dc magnetic field of 100 Oe was applied, and (iii) magnetization was recorded as temperature raised from 5 K → 300 K. The sample was further cooled down 300 K → 5 K under a magnetic field of 100 Oe to record the $M(T)$ magnetization in FC condition. The field-dependent magnetization $M(H)$ loops were measured within the ± 10 kOe range at 5 K. The EB and magnetic training effect measurements were conducted in the FC condition. To characterize the spin-relaxation dynamics and frequency dependence of the freezing temperature experimental data for the ac-magnetic susceptibility, in-phase $\chi'(\omega)$ and out-of-phase $\chi''(\omega)$ components were collected, employing excitation frequencies in the range of 50–300 Hz. During the ac-magnetic susceptibility measurements, an ac-drive field of 3.5 Oe was applied.

B. Computational details

All calculations were performed using spin-polarized density functional theory (DFT) [46] as implemented in the plane-wave-based code VIENNA AB-INITIO SIMULATION PACKAGE (VASP) [47] version 5.4. The kinetic energy cutoff for the plane waves was taken as 400 eV throughout the calculations. The structure models were relaxed for ionic positions at fixed experimental lattice parameters until the Hellmann-Feynman forces on each atom were less than 10^{-2} eV/Å, and the convergence criterion was taken as 10^{-6} eV. We used the generalized gradient approximation (GGA) for the exchange-correlation functional in the form of Perdew-Burke-Ernzerhof [48]. These materials do not have long-range dispersion; hence, the inclusion of any nonlocal correlation effect was discarded [49,50]. Strongly correlated transition-metal oxides exhibit localized d electrons with energy bands near the Fermi energy. Tradition local density approximations (LDAs) or GGA within the DFT framework often fail to describe the electronic and magnetic properties accurately [51]. Mixing a fraction of Hartree-Fock exchange in GGA corrects the delocalization error, but this method is computationally expensive [52–54]. A computationally feasible and efficient way to treat this overdelocalization is the rotationally invariant DFT + Hubbard U method, which corrects the on-site Coulomb interactions and allows significant improvement over LDA and GGA [55]. We varied the empirical
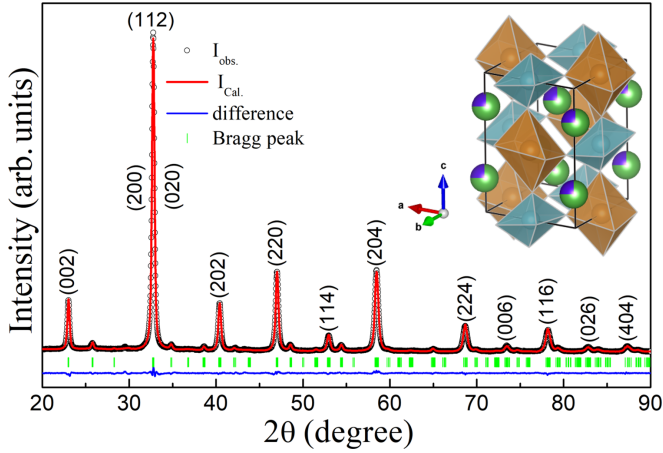
FIG. 1. Room-temperature XRD pattern of LSNMO where the black open circle, red line, blue line, and green sticks represent the raw data, fitted data, difference, and Braggs position, respectively. Inset shows the polyhedral picture of the unit cell where the green and blue balls represents the La/Sm and light blue and brown octahedra denote NiO_6 and MnO_6.

U parameter from 1–6 eV for the magnetic elements Mn and Ni to check the effect on the magnetic moments and electronic band gap. We found that 4 eV for both the Mn and Ni was used throughout the calculations because at 4 eV we got a reasonable band gap in our DFT calculation. We used the projected augmented wave potentials with $4f$ states of Sm atoms in the semicore state, which results in the valence electron for Sm: $5s^2\,6s^2\,5p^6\,5d^1$ and La: $5p^2\,6s^2\,5d^1$. Incorporating an f electron in the calculation may compromise the reliability of the results; hence the f electron is put in the semicore state as

described in earlier reports [56,57]. We used the following valence electronic configurations for Ni: $4s^1\,3d^9$; Mn: $4s^1\,3d^6$; and O: $2s^2\,2p^4$, respectively. The $6\times6\times4$ Monkhorst-Pack set of **k** points were used for the Brillouin zone integration for the unit cell of 20 atoms and scaled proportionally in supercell calculations for better energy comparisons [58]. We doubled the **k** points in the self-consistent calculations to produce the density of states (DOS) in respective magnetic configurations. The investigation of partial oxidation states is conducted employing the grid-based Bader approach. However, it is crucial to note that obtaining quantative charges for perfect oxidation states is limited in this approach [59].

III. RESULTS AND DISCUSSION

A. Structural analysis

Figure 1 shows the XRD pattern and Rietveld refinement with the FULLPROF SUITE for the 2θ range of 20–90°. The crystal structure of LSNMO has been indexed as monoclinic symmetry (space group: $P2_1/n$), except for a negligible fraction of impurities as seen across 30°. Table I shows the structure parameters obtained from the refinement. It is important to note that parent compounds of this material, $LaMnO_3$, $LaNiO_3$, and $SmNiO_3$ crystal structures belong to orthorhombic (space group: $Pnma$), rhombohedral (space group: $R\bar{3}c$), and orthorhombic (space group: $Pbnm$) categories, respectively [60–62]. The compounds related to LSNMO are also marked in Table I. LSNMO compound transforms the crystal structure towards a lower symmetry, i.e., monoclinic due to the substitution of La with Sm (or Ni with Mn) and induced octahedral distortions. The lattice parameters of the monoclinic system are 5.4650, 5.4625, and 7.7400 Å, and the angle (β) is equal to 89.768°. The fitting parameters R_{wp}, χ^2 and

TABLE I. Room-temperature lattice parameter, bond length (Å), bond angle (°), and atomic position driven from Rietveld analysis of LSNMO. XRD pattern and their comparison with related to parent compound.

Lattice parameters (monoclinic crystal structure $P2_1/n$ space group)							
a (Å)	b (Å)	c (Å)	α (°)	β (°)	γ (°)	V (Å³)	χ^2
5.4650(1)	5.4625(6)	7.7400(1)	90	89.7683(4)	90	231.06	2.3

a (Å)	b (Å)	c (Å)	β (°)	Compound		Space group	Ref.
5.3638(5)	5.8517(5)	7.4825(5)	90	$SmMnO_3$		$Pnma$	[64]
5.4941 (4)	5.4941 (4)	13.3122 (2)	90	$LaMnO_3$		$R\bar{3}c$	[65]
5.525	5.484	7.767	90.02	La_2NiMnO_6		$P2_1/n$	[63]
5.35647(11)	5.52127(11)	7.61932(17)	90.030(26)	Sm_2NiMnO_6		$P2_1/n$	[66]
Bond length and bond angles							

La/Sm–O (Å)	Ni–O1 (Å)	Ni–O2 (Å)	Ni–O3 (Å)	Mn–O1 (Å)	Mn–O2 (Å)	Mn–O3 (Å)
2.7165	1.9900	2.0504	1.5329	1.9680	1.8829	2.3430
	Ni–O1–Mn (°)		Ni–O2–Mn (°)		Ni–O3–Mn (°)	
	154.904		158.361		173.552	
			Atomic position			

	x	y	z
La/Sm (3+)	−0.0011	0.0250	0.2485
Ni (2+)	0.5	0	0
Mn (4+)	0	0.5	0
O1 (2−)	0.2736	0.2768	0.0494
O2 (2−)	0.2135	0.1914	0.5040
O3 (2−)	0.4828	−0.0082	0.1973

goodness of fit are 5.00, 2.35, and 1.6, respectively. Structural refinement findings suggest that Ni–O (Mn–O) bond length and Ni–O–Mn $\neq 180°$ bond angle are distinct from ordered LNMO that serve as a microscopic mechanism of the orbital distortion in the crystal structure [20,29,63]. The degree of orbital distortion originates magnetic competition and geometrical frustration in disordered perovskite systems [20,26–29,63].

The inset of Fig. 1 depicts the crystal structure of LSNMO. The Ni(Mn) cations are octahedrally coordinated by six oxygen atoms and constitute NiO_6 (light blue) and MnO_6 (brown) octahedra that are situated either at (1/2, 0, 0) or (0, 1/2, 0) positions across the crystallographic directions. The brightest peak is recorded across 33°, corresponding to the (112) plane reflection. This indicates that the corner-shared NiO_6 and MnO_6 octahedra are not arranged alternately across the entire lattice uniformly, which further originates a possible source of ASD in the LSNMO. The detailed characteristics of structural ASD on the ground spin states are further explored by magnetization measurements in the following sections.

B. Temperature-driven magnetic transitions

Magnetic transitions and ground-state magnetic properties of LSNMO are explored by magnetization versus temperature $M(T)$ measurements in zero-field-cooled (M_{ZFC}) and field-cooled (M_{FC}) conditions using external magnetic fields (H_{dc} = 100, 500 Oe) as shown in Fig. 2(a). The major finding of the $M(T)$ curves can be highlighted as follows: (i) the magnetization increases from 243 K for both M_{ZFC} and M_{FC} curves, (ii) different rates of change for M_{ZFC} and M_{FC}, (iii) a bifurcation in the M_{ZFC} and M_{FC} magnetization curves across the irreversibility temperature T_{ir} = 243 K, and (iv) the notable difference between M-T curves [see Fig. 2(a)] in paramagnetic (PM) regions indicates a Griffiths-like phase or any other type of short-range correlation above Curie temperature. The presence of disorder transforms this long-range cationic ordering into a short-range order phase. All reported characteristics of $M(T)$ curves show resemblance with conventional magnetic frustrated systems such as canonical SG, cluster SG, and superparamagnetic (SPM) phase [9,19,31].

The presence of mixed valence states of $Ni^{2+/3+}$ and $Mn^{3+/4+}$ cations promotes multiple magnetic exchange interactions: (i) FM superexchange interaction $Ni^{2+}(e_g^2)$–O^{2-}–$Mn^{4+}(e_g^0)$; (ii) $Ni^{2+}(e_g^2)$–O^{2-}–$Ni^{2+}(e_g^2)$ and $Mn^{4+}(t_{2g}^3)$–O^{2-}–$Mn^{4+}(t_{2g}^3)$ AFM interactions; (iii) Ni^{3+} LS(e_g^0)–O^{2-}–Mn^{3+} HS(e_g^1) (LS: low spin, HS: high spin) cations driven superexchange FM interaction; (iv) AFM superexchange between pairs Ni^{3+} LS(e_g^1)–O^{2-}–Ni^{3+} LS(e_g^1) and Mn^{3+} HS(e_g^1)–O^{2-}–Mn^{3+} HS(e_g^1); (v) $Ni^{2+}(e_g^2)$–O^{2-}–$Ni^{3+}(e_g^1)$ double-exchange interaction; and (vi) $Mn^{3+}(e_g^1)$–O^{2-}–$Mn^{4+}(e_g^0)$ ordering driven FM double exchange interaction [20,25,29,63]. All these competing exchange interactions that can modulate the local octahedral distortion as Mn^{3+} are Jahn-Teller active cations. LSNMO systems have a dominating fraction of the cation-ordered phase and mentioned interactions (i) and (iii). However, Ni^{3+} LS–O^{2-}–Mn^{3+} HS superexchange interaction is less likely to participate in the formation of the ground state. These competing exchange interactions lead to multi-
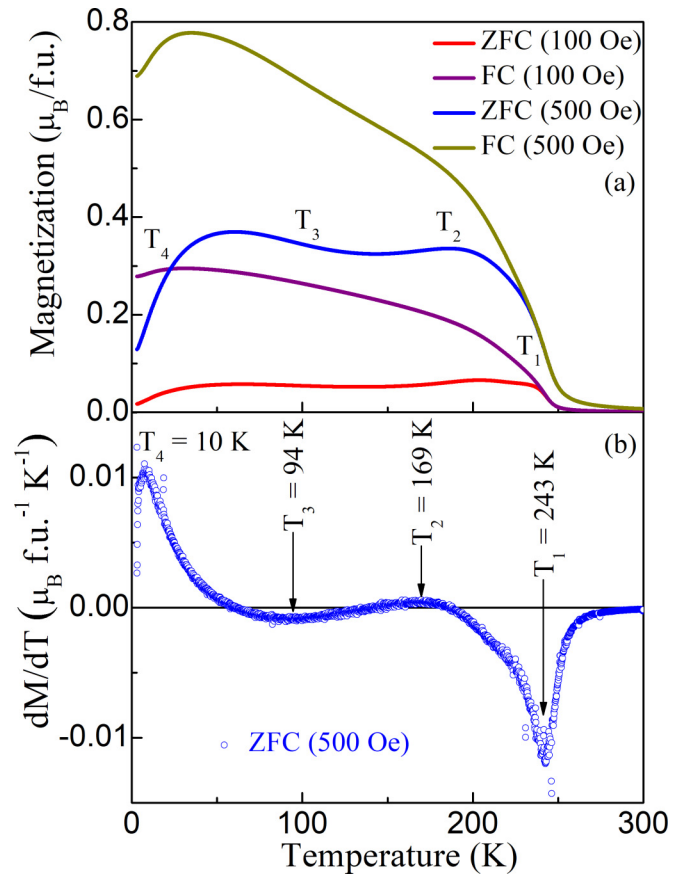

FIG. 2. (a) ZFC/FC magnetization curves recorded under an applied external magnetic field of 100 and 500 Oe; (b) dM/dT for dc magnetization in ZFC protocol at 500 Oe field value.

ple magnetic anomalies as observed previously [20,29,63]. The ordering temperatures of the LSNMO compound can be deduced from the derivative of M_{ZFC}, i.e., (dM_{ZFC}/dT) as shown in Fig. 2(b). The transition across 243 K represents the PM→FM phase transition at temperature (T_{C1}), attributed to the Ni^{2+}–O^{2-}–Mn^{4+} exchange interaction. The pronounced value of M_{ZFC} indicates a strong FM coupling between the Ni^{2+}/Ni^{3+} and Mn^{4+}/Mn^{3+} spins as marked in Fig. 2(b). There is a plethora of literature about the presence of multiple charge valences with their fraction that can be estimated by XPS [29,33,67–72]. At lower temperatures, the dominating AFM coupling is evident in the ZFC curves.

The effective magnetic moment (μ_e) of the ordered LSNMO compound can be estimated using formula $\mu_e = \mu_B \sqrt{x(\mu_{Mn^{4+}})^2 + (1-x)(\mu_{Mn^{3+}})^2 + y(\mu_{Ni^{2+}})^2 + (1-y)}$

$(\mu_{Ni^{3+}})^2 + 0.5(\mu_{Sm^{3+}})^2$, where $\mu_{Mn^{3+/4+}}$, $\mu_{Ni^{2+/3+}}$, and $\mu_{Sm^{3+}}$ are the magnetic moments for their respective HS $Ni^{3+}(3d^7, S = 3/2)/Ni^{2+}(3d^8, S = 1)$, or $Mn^{4+}(3d^3, S = 3/2)/Mn^{3+}(3d^4, S = 2)$, La^{3+} $(5d^0)$, and Sm^{3+} $(4f^5, J = 5/2)$; x and y are the phase fractions of Mn^{4+} and Ni^{2+}. For compound LSNMO, the values for x = 0.51 and y = 0.56 are obtained from the XPS study (see Supplemental Material Ref. [73]). The theoretical value for the magnetic moment for Sm can be calculated by equation $\mu = g\sqrt{J(J+1)}$. Considering $g = 0.285$, the obtained value for $\mu_{Sm^{3+}}$ = 0.85 μ_B. The theoretical value for the magnetic moment for Mn(Ni) in their high

spin states can be estimated by using $\mu_{Mn(Ni)} = g\sqrt{S(S+1)}$. $g = 2$ for Mn and Ni cations give rise to $\mu_{Mn^{4+}} = 3.87 \mu_B$, $\mu_{Mn^{3+}} = 4.90 \mu_B$, $\mu_{Ni^{3+}} = 3.87 \mu_B$, and $\mu_{Ni^{2+}} = 2.83 \mu_B$. For a perfectly ordered LSNMO compound $\mu_e = 5.55 \mu_B$, which is larger than the observed magnetic moments ($\mu_o \approx 3.83 \mu_B$). The notable difference between calculated effective and observed magnetic moments indicates the presence of a prominent fraction of disorder sites [20,29,31,32,37].

The magnetic irreversibility in M_{ZFC} and M_{FC} across 243 K corresponds to magnetic frustration that will be explored in further detail by magnetic memory and training effects in the following sections. The other three notable anomalies at T_2 (169 K), T_3 (94 K), and T_4 (10 K) in M_{ZFC} can be clearly visualized [see Fig. 2(b)] for the LSNMO system. Across T_2, the AFM interaction is dominant because of the dominating antisite disorder that suppresses the saturation magnetization. The wide transition across T_3 corresponds to phase separation representing the coexisting FM and SG phase [31]. Murthy *et al.* observed that double perovskite La$_{2-x}$Sr$_x$CoMnO$_6$ ($x = 0.1 - 0.5$) displays an antisite-disorder driven SG state [31]. The ZFC curve and large anisotropy between ZFC and FC curves at $T_4 = 10$ K suggest a frozen AFM transition that plays a major role in governing the EB effect in such a magnetic frustrated system [31]. Additional anomalies reported across $T_3 = 94$ K and $T_4 = 10$ K mainly reflect the presence of antisite disorder and competing exchange interactions in the system. In contrast, the ordered parent LNMO displays an FM transition around $T_{C1} \sim 280$ K due to the order spin state of Ni^{2+} and Mn^{4+} ions, however, for a disordered phase exhibits an additional FM transition around $T_{C2} \sim 150$ K for the Ni^{3+}/Mn^{3+} magnetic phase with SG ordering across 38 K [20,25,29,63].

C. Isothermal magnetization and critical analysis

A detailed exploration of the magnetic transition and nature of involved exchange interactions in LSNMO compound are analyzed using scaling formalism of a set of exponents β, γ, and δ. Generally, exponents β and δ are estimated from M_s and magnetic susceptibility $\chi_0(T)$ in the proximity of T_c, while δ is an isothermal exponent. These critical exponents are correlated with M through the following expression:

$$M_s(T) = M_0(-\varepsilon)^\beta; \quad \varepsilon < 0, T < T_c, \quad (1)$$

$$\chi_0(T)^{-1} = (h_0/M_0)\varepsilon^\gamma; \quad \varepsilon > 0, T > T_c, \quad (2)$$

$$M = DH^{1/\delta}; \quad \varepsilon = 0, T = T_c, \quad (3)$$

where $\varepsilon = (T-T_c)/T_c$ reflects the reduced temperature, and M_0, h_0/M_0, and D are critical amplitudes. β, γ, and δ are the critical exponents that are associated with $M_s(T)$, $\chi_0(T)^{-1}$, and T_c [74–76]. These corresponding critical exponents can be collectively expressed using equation $(H/M)^{1/\gamma} = (T-T_c)/T_c + (M/M_1)^{1/\beta}$, where M_1 is a constant and $M_s(T)$ and $\chi_0(T)^{-1}$ are deduced from the high field region. Figures 3(a) and 3(b) illustrate the isotherm $M(H)$ across 227–275 K and H/M vs M^2 plots. The positive slopes in H/M vs M^2 plots suggest that PM → FM is a second-order transition as evident from Arrott plots, which are nonlinear. The critical exponents ($\beta = 0.5$ and $\gamma = 1.0$) are estimated using the mean-field theory model
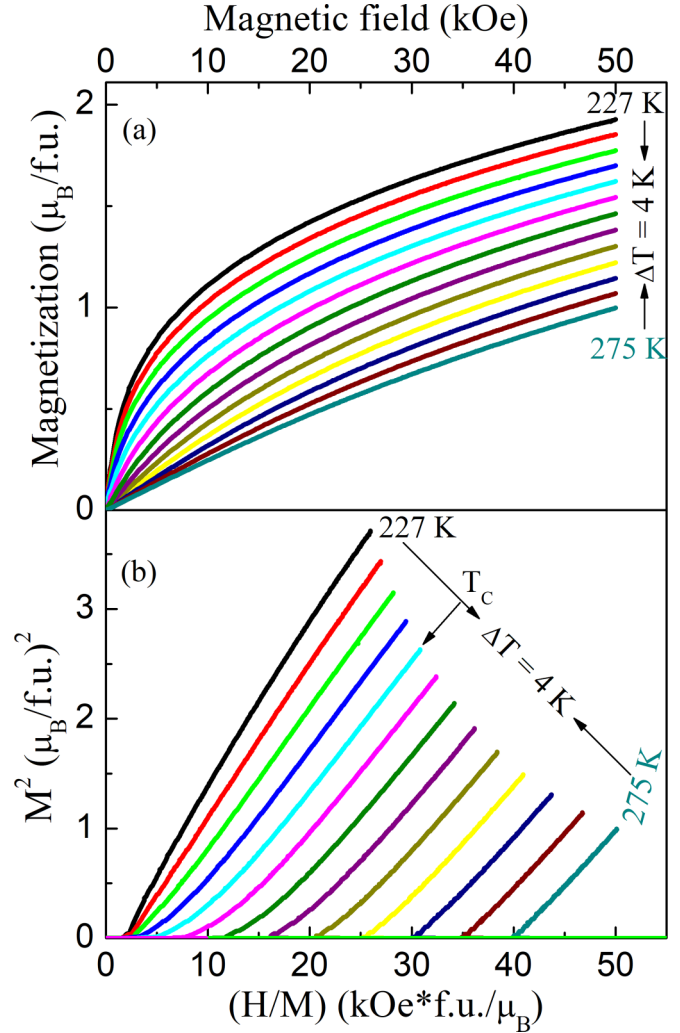

FIG. 3. (a) M-H plots of LSNMO between 227 K to 275 K (in 4 K steps); (b) Arrott plots of M^2 vs (H/M) at a different temperature around T_C.

[74,75]. The mean-field theory model across T_c, M^2 vs H/M at multiple temperatures displays a series of parallel lines at $T = T_c$ that intersect through the origin [74–76]. The curves across T_c can be extended sharply into the H/M axis to yield reliable values of the M_s (T, 0) and $1/\chi_0(T)$.

D. Isothermal magnetization loop

To access the additional details of the magnetic ground state, we measure isothermal magnetization $M(H)$ loops up to ± 15 kOe across 5–300 K as shown in Fig. 4. The right inset shows the pristine $M(H)$ curve from $0 \rightarrow 50$ kOe collected at 5 K, indicating a saturated magnetization with coercive field $H_C = 1.2$ kOe. The $M(H)$ loop characteristics indicate the coexisting FM and AFM phases in the low-temperature region, excluding the presence of any SPM phases or blocking magnetic moments. At 300 K, the $M(H)$ loop confirms the PM phase as evident by the straight line shape of the $M(H)$ loop with negligible H_C and remanent magnetization (M_r) that also confirms the absence of any other magnetic impurity phases [23,24]. Using the pristine $M(H)$ loop, theoretically, the value of M_s estimated in the high magnetic field region ($H = 20$-50
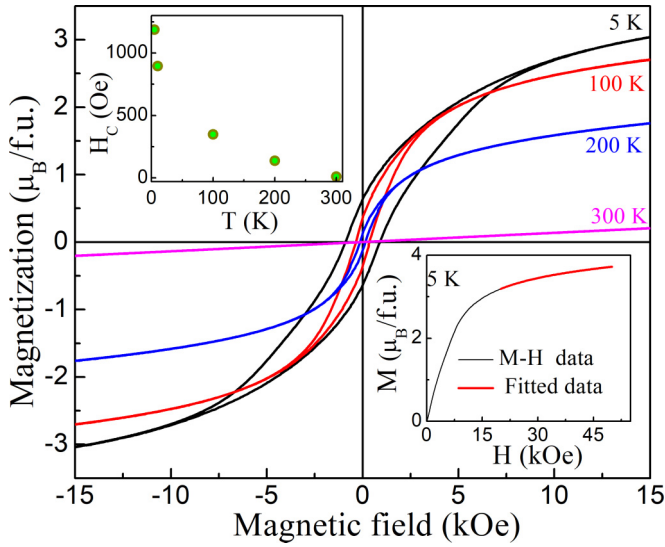
FIG. 4. ZFC isothermal magnetization at 5 K, 100 K, 200 K, and 300 K. The left inset shows the variation of a coercive field with temperature, and the right inset shows pristine $M(H)$ loops at 5 K up to +50 kOe.

kOe) through using the relation $M(H) = M_s[1 - \frac{a}{H} - \frac{b}{H^2}] + cH$, where c is the high magnetic field differential susceptibility, a is nonmagnetic inclusion of local magnetic moments, and b reflects the magnetocrystalline anisotropy of the system [see inset of Fig. 4]. The observed value of M_s for LSNMO is approximately 3.83 μ_B/f.u.

The temperature-dependent H_C of LSNMO compounds is shown in Fig. 4 (left inset). The reduced value of M_s indicates a prominent fraction of ASD induced by mixed valence states of Ni (Ni^{2+}/Ni^{3+}) and Mn (Mn^{3+}/Mn^{4+}). The mismatch in the simulated to experimentally reported M_s values directly indicates the prominent presence of ASD [29,76–78]. In an ordered LNMO, each transition cation (Ni/Mn) is surrounded by six neighboring transition metal ions Ni/Mn and displays FM correlation [15,24]. For a disordered LSNMO, one Ni ion can be surrounded by five Mn and one Ni ion. A similar scenario is also considered for Mn ions. Therefore, such disordered LSNMO results in Mn^{3+}–Mn^{3+}, Mn^{3+}–Mn^{4+}, Mn^{4+}–Mn^{4+}, Ni^{2+}–Ni^{3+}, Ni^{2+}–Ni^{2+}, and Ni^{3+}–Ni^{3+} disorder pairs while every ordered site creates Ni^{2+}–Mn^{4+} and Ni^{3+}–Mn^{3+} pairs. The disordered and ordered pairs induce AFM and FM exchange interactions, respectively. These mutually competing exchange interactions result in a reduced magnetic moment in the presence of ASD [29].

E. Exchange bias and magnetic training effect

The multiple short-range exchange interactions instigate magnetic frustration and random pinning centers across APB in the SG state. The EB effect across APB in the SG phase has been reported in various likewise systems under field-cooled conditions [24,30,31,38]. These findings motivate us to explore the magnetic frustration, spin-relaxation dynamics, and EB effect in the SG state of the LSNMO system. To measure the EB field, $M(H)$ loops are recorded at 5 K in FC conditions with $H_{max} \leqslant \pm 10$ kOe, which allows excluding
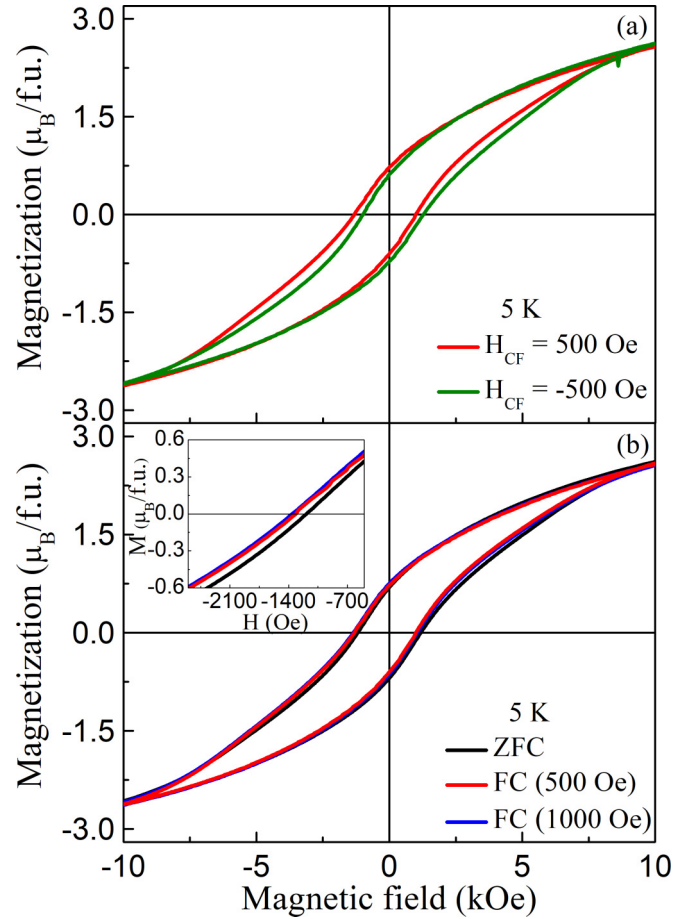

FIG. 5. (a) $M(H)$ loops measured at 5 K after cooling the sample from 300 K under a magnetic field of +500 Oe (red line), and −500 Oe (green-line) representing the presence of exchange bias. (b) $M(H)$ loop measured at 5 K ZFC and FC mode in the presence of different cooling fields (0, 500, 1000 Oe). Inset shows the enlarged view.

any minor loop effects [see Fig. 5(a)]. The $M(H)$ loop recorded in field-cooled condition with cooling field (H_{CF}) +500 Oe is found to be shifted towards the negative field direction in comparison to the centered $M(H)$ loop recorded in ZFC. The $M(H)$ hysteresis loop recorded with $H_{CF} = -500$ Oe drifted in the reverse direction. These observations of the shift in $M(H)$ loops $H_{CF} = \pm 500$ Oe of the hysteresis loop is considered the direct evidence of the EB effect. To monitor the EB variation as a function of cooling field strength H_{CF}, we recorded the $M(H)$ under the following protocol: cool down the system from the PM state to 5 K under cooling field $H_{CF} = 500$ Oe and then recorded the $M(H)$ loops for the range ± 10 kOe. The measured $M(H)$ loops are found to drift along the negative field direction that terms as the EB effect [5,6]. It is also significant to mark that the LSNMO system does not display any shift in $M(H)$ loops recorded in the ZFC condition. The $M(H)$ loops acquired with only FC conditions are shifted with magnitude $H_{EB} = (H_{C1} + H_{C2})/2$ where $H_{C1}(H_{C2})$ is ascending (descending) coercive fields [34–36,79–81]. Figure 5(b) shows the variation of the EB with the magnetic field $M(H)$ for different strengths of H_{CF}. The increasing shift for H_{CF} being 500 and 1000 Oe is visible in the inset. Similar observations

have been also reported for compounds $Sm_{1.5}Ca_{0.5}CoMnO_6$ [23], and $LaSrCoFeO_6$ [24]. The observed H_{EB} and corresponding coercive field H_C for cooling field $H_{CF} = 500$ Oe were ~ 153 Oe and ~ 1.2 kOe for the LSNMO compound.

The EB effects have been studied for the SG phase arising from the competing FM and AFM exchange interactions [5,6,24]. This magnetic frustrated ground phase reported in the various compounds such as $LaSrCoFeO_6$ [24], $La_{2-x}Sr_xCoMnO_6$ [31], and $LaFeO_3$ [82] perovskites show the notable EB effect. During magnetic field cooling, the SG spins aligned along the H_{CF} direction and within the range of $0 \leqslant H_{CF} \leqslant 10$ kOe the M_s of the FM state is relatively smaller and corresponding unidirectional anisotropy is larger. Further increasing H_{CF} increases the fraction of the FM state that will eventually dominate the magnetic ground state. The major fraction of the FM state reduces the contribution of unidirectional anisotropy in the SG state across FM/AFM boundaries. Hence, the ground-state spin configuration of the LSNMO compound is a collective state of three different competing magnetic phases, i.e., the SG state, AFM order, and field-driven FM phase.

The magnetic training effect that corresponds to a continuous reduction of the H_{EB} with successive magnetic-field reversal is explored for magnetic heterogeneous LSNMO compound. The training effect is mainly characterized by a suppression of EB strength through modulating the spin torque imparted by pinning boundaries in the SG state of LSNMO. Depending on the number of cycles (n), H_{EB} reduces sharply after the first cycle and continuously converges towards a threshold value in the following cycles. Numerous empirical models have been proposed to describe the training effect and reduction of H_{EB} as a function n. It is widely accepted that during field cooling, such frustrated compounds persist in multiple FM clusters in an AFM matrix or vice versa. The sharp reduction in H_{EB} and its variation with field cycles can be described within the framework of an empirical power law, i.e., $\Delta H_{EB} \, \alpha \, n^{-1/2}$ with $n > 1$. A magnetic training effect is a direct approach that provides the intrinsic EB effect in the form of spin rearrangement and their relaxation across pinning interfaces [81,83]. The spin rearrangement instigates a reduction in magnetic anisotropy and hence steadily lower H_{EB} as a function of n. We recorded in total 13 sequential $M(H)$ loops at 5 K with $H_{CF} = +1000$ Oe and the sweeping magnetic field range ± 10 kOe.

Figure 6(a) highlights the $M(H)$ loops for the negative field quadrant for successive cycles $n = 1, 2, 4, 7, 10,$ and 13. Figure 6(b) shows the training effect as confirmed by the nonmonotonous reduction of $H_{EB}(n)$. Similar features of H_{EB} have been also reported for other SG systems exhibiting the spin relaxation and modification of AFM spins pinning strength due to magnetization reversal [18,83]. For the LSNMO system, a significant change of H_{EB} ($\sim 67\%$) has been noticed in between the $n = 1 \rightarrow n = 2$ cycles [shown in Fig. 6(b)]. However, only 6% change in H_{EB} is noticed from $n = 2 \rightarrow n = 3$ cycles. This prominent reduction of H_{EB} suggests that across the pinning boundaries, a finite fraction of pinned spins promptly reverse or flip with the external applied magnetic field [83]. Therefore, the frustrated spin state with dominating the pinning boundaries driven instability of
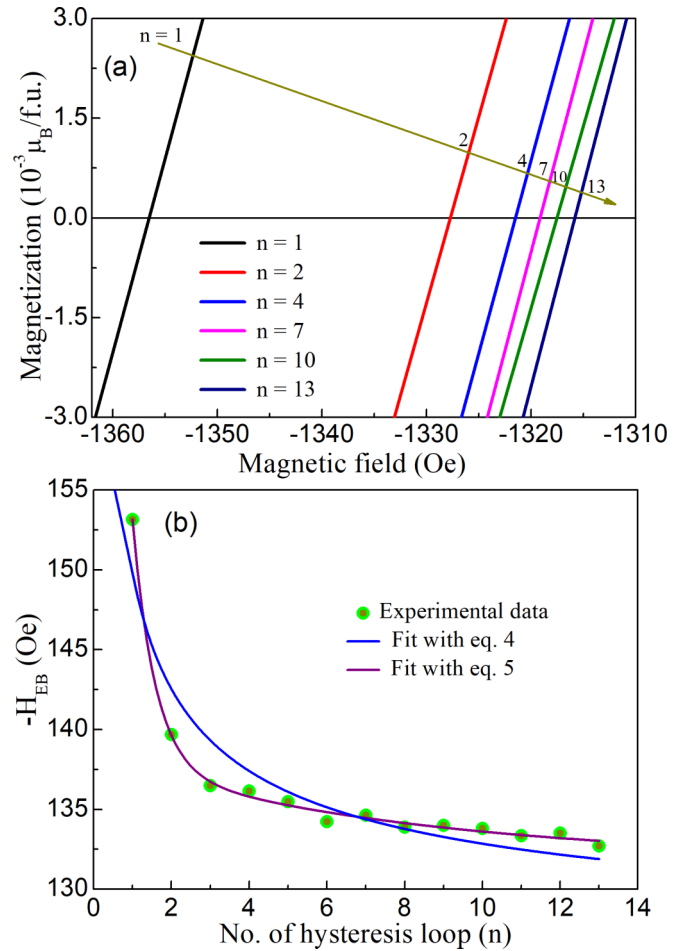

FIG. 6. (a) The zoomed view of hysteresis loop at 5 K after 1000 Oe cooling field with 13 continuous cycles (magnetic training effect for EB). (b) The number of loops (n) dependent on H_{EB} extracted from training at 5 K. The blue solid line represents the best fit using empirical power law and the purple solid line represents the best fit as proposed by Ref. [18].

interface and H_{EB} as a function of n can be explained using the following empirical law [81,83,84]:

$$H_{EB}(n) - H_{EB}(\infty) \propto \frac{1}{\sqrt{n}}, \quad (4)$$

where H_{EB} (∞) is the H_{EB} value for $n \rightarrow \infty$. The solid line in Fig. 6(b) shows the best fit of H_{EB} for $n = 1$ to $n = 13$. The best fitting parameters observed from numerical analysis using Eq. (4) is $H_{EB}(\infty) = 125$ Oe. The monotonous reduction of $H_{EB}(n)$ is mainly driven by the relaxation of magnetic anisotropy across the pinning boundaries in the SG phase that is significantly influenced by the rotating and frozen spins in the frustrated state. However, the empirical power-law approach only explains the dissipative energy of the AFM spins across the FM/AFM pinning boundaries. Therefore, it is difficult to capture the entire details related to the change of H_{EB} as a function of n using the empirical law expressed in Eq. (5). Recently, a suitable model was proposed to describe the training effect by considering both irreversible (frozen) and reversible spins for such magnetically inhomogeneous

SG-like phases [18]. The expression for this approach can be described as

$$H_{EB}(n) - H_{EB}(\infty) = A_f * \exp\left(-\frac{n}{P_f}\right) + A_r * \exp\left(-\frac{n}{P_r}\right),$$

(5)

where A_f and P_f are the parameters associated with the modification of the frozen spins, and A_r and P_r are parameters representing the reversible (rotatable) spin fractions of the frustrated spins across pinning boundaries of SG phases. From the fitting of H_{EB} data, the resulting parameters are $H_{EB}(\infty) = 131.8 \pm 1.8$ Oe (similar value obtained from empirical law), $A_f = 87.68 \pm 17.72$ Oe, $P_f = 0.57 \pm 0.09$, $A_r = 6.53 \pm 0.82$ Oe, and $P_r = 7.82 \pm 6.17$. Comparing the ratio between P_f and P_r suggests modifications in the relaxation characteristics of both irreversible (frozen) and reversible (rotatable) spin fractions. In this paper, we observe that the value of P_r is much higher than P_f, which indicates that the reversible spin relaxes approx. ~ 14 times faster in comparison to frozen spins across pinning FM/AFM boundaries in the SG state. Identical magnetic training effect has been reported in various other systems, including $Sm_{1.5}Ca_{0.5}CoMnO_6$ [23] and $LaSrCoMnO_6$ compounds [24].

F. Spin-glass dynamics

Further exploration of dynamics is done by monitoring the frequency-dependent (50–300 Hz) ac susceptibility (χ') in the temperature range of 20–250 K. Figure 7(a) shows the multiple cusps, each representing the magnetic transitions visible in χ'. Figure 7(a) clearly shows cusps in χ' at each magnetic transition indicated in Fig. 2(a). The inset of Fig. 7(a) shows the frequency-dependent maxima of the cusp at low temperature located in the SG phase that shows a continuous shift towards the higher temperature side as frequency increases. This shift induced through an extension of the action time-mediated spin relaxation delay is considered intrinsic evidence of the SG phase. Generally, the Mydosh parameter $\Omega = \frac{1}{T_f(\omega)} * \frac{\Delta T_f(\omega)}{\Delta \ln \omega}$ is used to differentiate the various microscopic origin and mechanism of the spin relaxation and associated dynamics [9,19]. $\Delta T_f(\omega)$ represents the peak shift of such a cusp as a function of frequencies. Typically, for a magnetic frustration derived through cluster glass freezing, the value of Ω ranges from 0.005 to 0.09, whereas, for the frustration mediated through SPM phases, Ω is usually extended between 0.1–0.3 [9,19,63]. For the LSNMO compound, the estimated $\Omega = 0.013$ indicates a dispersion in frequency-dependent χ' that mainly originates from the SG system [9,19]. This method is also used to exclude any feasibility of the SPM phase [9].

These interacting cluster SG systems are best explained by applying various empirical models to establish the link between the frequency (ω) and the characteristic relaxation time (τ). The τ associated to the peak temperature $T_f(\omega)$ for every measured frequency $\omega = 2\pi f$ was estimated utilizing expression $\tau = 1/2\pi f$ [9,19,24,63]. The power-law behavior, which indicates critical slowing down, has been used to understand the relaxation mechanism [24,63]. The cluster SG systems and associated critical spin-freezing dynamics can also be analyzed by employing the Vogel-Fulcher (VF) formalism using the expression $\tau = \tau_0 * \exp(\frac{E_a}{k_B[T - T_{VF}]})$, where, E_a denotes
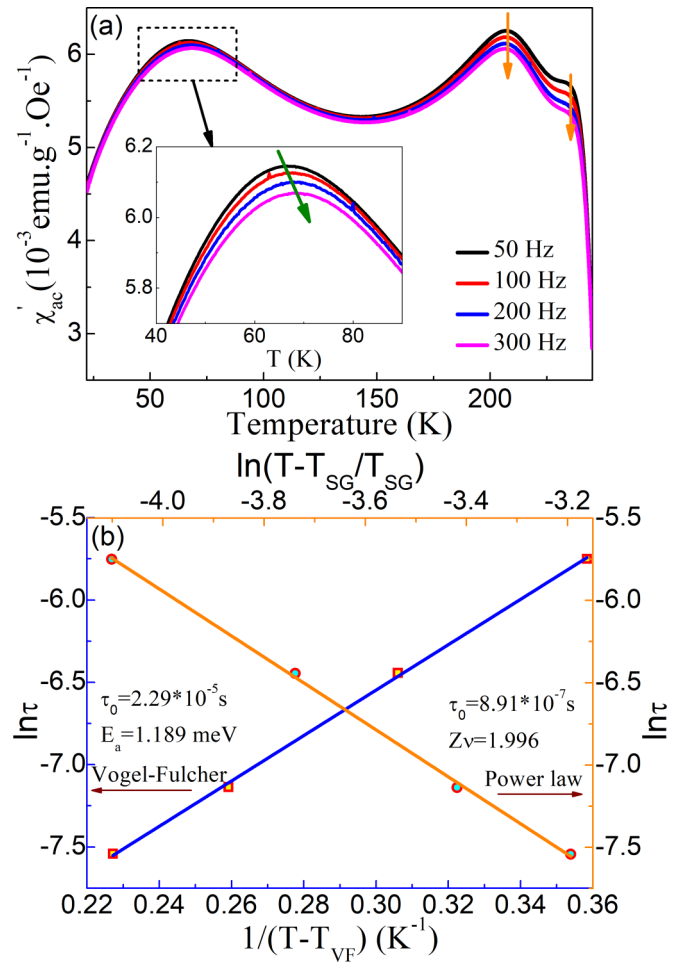

FIG. 7. (a) Real part of ac-susceptibility variation with the temperature at different frequencies 50, 100, 200, and 300 Hz. Inset shows an enlarged view of cusp shifting, (b) $\ln(\tau)$ versus $\ln(T/T_{SG}-1)$ and $1/(T-T_{VF})$ plots for sample LSNMO, wherein the blue and orange solid lines represent the best fits of Vogel-Fulcher and power law, respectively.

the activation energy, k_B is Boltzmann constant, and T_{VF} is the freezing temperature at which the spin dynamics manifest the dispersion and carries a resemblance to the T_{SG} [9,19,63]. Commonly, the frustrated state through critical slowing down approaches the relaxation reflects a linear characteristic for $\ln(\tau)$ vs $1/(T-T_{VF})$ plot [9,19,63]. The VF formalism provides a good quality fit as appears from a line plot through the data points in Fig. 7(b). The observed simulated fitting parameters for VF law are $T_{VF} = (64.2 \pm 0.1)$ K, $E_a = 1.189$ meV, and $\tau_0 = 2.29 \times 10^{-5}$ s. It is important to mention that the value of activation energy is comparable to the activation energies reported for the other frustrated cluster SG systems [9,19,85].

The spin dynamics and associated dispersion across T_{SG} are used to explore further details and model the frequency dependence of the SG freezing temperature $T_f(\omega)$. The reported dispersion at T_{SG} can be described using the expression $\tau = \tau_0(\frac{T_f(\omega) - T_{SG}}{T_{SG}})^{-z\nu}$, where τ_0 denotes the characteristic relaxation time, T_{SG} is the SG transition temperature where τ shows the divergence, and ν is the critical exponent representing the correlation length $\xi = (\frac{T_f}{T_{SG}} - 1)^{-\nu}$, where z terms

are the dynamic exponents that can be expressed as $\tau \sim \xi^z$ [9,19,63]. The numerical analysis of $\ln(\tau)$ with respect to $\ln(\frac{T_f}{T_{SG}} - 1)$ plot illustrated as a solid line in Fig. 7(b) provides $T_{SG} = 65.9$ K, $\tau_0 = 8.91 \times 10^{-7}$ s, and $z\nu = (1.996 \pm 0.04)$. The reported higher value of τ_0 indicates a slower dynamic as predicted from a cluster SG system, where τ_0 typically ranges $\sim 10^{-6}$–10^{-10} s. Higher values of τ_0 have also been reported in various other systems like magnetite and perovskite nanoparticles [9,19,74]. For canonical SG systems such as CuMn, the value of τ_0 is in of the order of $\sim 10^{-13}$ s that is significantly lower in comparison to the cluster SG system [9,19,85]. Thus, both the power-law and VF approaches confirm the cluster SG freezing with $T_{SG} \sim 65 \pm 1$ K.

G. Magnetic memory effect

The spin-relaxation process and magnetic memory effect displayed by these frustrated SG systems alternatively can also be explored by measuring the time-dependent magnetization M_t [86]. Depending on the magnetic ground state, a relaxation of frustrated spins toward equilibrium stable spin configuration leads to a slow reduction of M_t value [86]. Usually, cluster SG systems show memory and rejuvenation effects due to the degenerated ground state. To monitor the memory effect, the first LSNMO sample field is cooled from 300 K $\rightarrow$ 5 K under $H_{CF} = 100$ Oe and a step followed by a warming thermal cycle to record $M(T)$ in the presence of the field is labeled FCW$_{ref}$. After approaching 300 K, the sample follows a cooling cycle under the same field and records $M(T)$, but briefly stops for a waiting time of 1 h at $T = 50$ K and 25 K. During the waiting period, the magnetic field is set to zero, then reapplied and the cooling is resumed [87,88]. This magnetization measurement is labeled FCC$_{stop}$. After cooling the system at 5 K, the warming cycle with the same applied field (100 Oe) follows along the $M(T)$ measurement without any intermediate stops and is termed FCW$_{memory}$. Figure 8(a) manifests the memory effect curve that exhibits steplike characteristics below T_{SG}. The steplike feature is a direct confirmation of the memory effect that is significantly prominent for the heating cycle curves where the step is completed. The manifestation of the memory effect also indicates the presence of an inhomogeneous SG system. This paper presents exclusive evidence of the existence of magnetic frustration in the form of SG using multiple criteria. The slow relaxation dynamics of thermoremnant magnetization below the SG transition in cluster SG state has been a debated topic, leading to a plethora of theoretical and experimental investigations.

For an interacting cluster SG system, the M_t should exhibit a stretched exponential behavior which is proposed by a generalized formula $M_t = M_0 + M_r * \exp(-\frac{t}{\tau})^{1-\alpha}$, where M_0 is the characteristic magnetization component, M_r denotes remanent magnetization of a glassy state, τ is the relaxation time, and α represents the stretched exponent [87–89]. For SG systems, the numerical value of α mostly extends from 0 and 1. $\alpha = 0$ indicates mono-dispersive Debye-like relaxation dynamics, and $\alpha = 1$ represents the lack of any relaxation. The mean range $0 < \alpha < 1$ indicates a non-Debye nature with relaxation times that emerge in the presence of a large number of degenerate states in the magnetic frozen phase. Employing
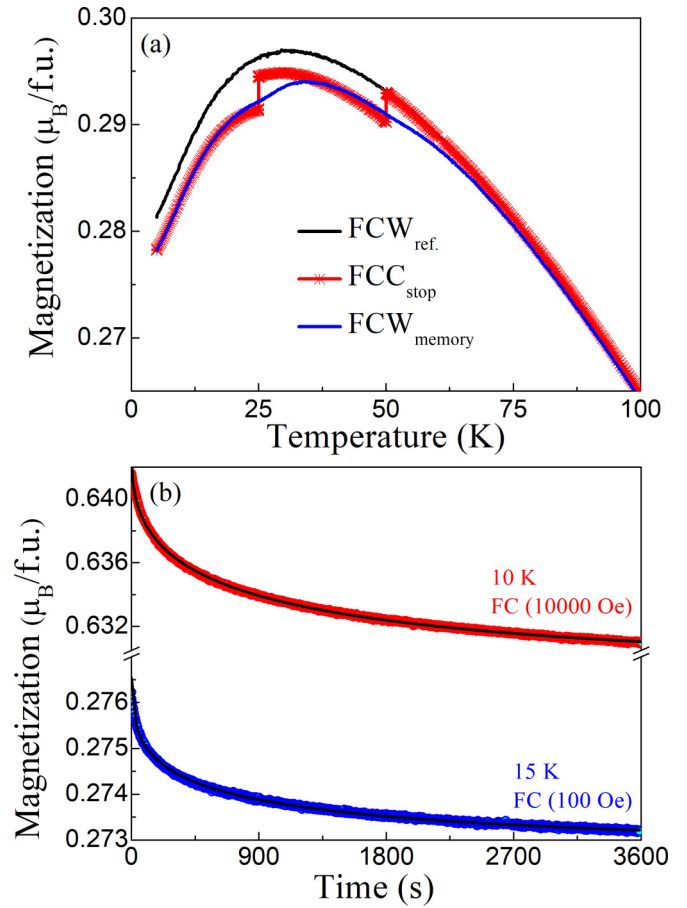

FIG. 8. Temperature-dependent FC magnetization data during memory measurement. (b) Magnetic relaxation measurement at a different field and temperature; the black line represents the best fit using the stretched exponent function.

the generalized exponential function, in this section, we understand the slow relaxation of the glassy phase of LSNMO. To measure this, the sample was first cooled from 300 $\rightarrow$ 10 K under 10 kOe external magnetic field. Afterward, the magnetic field was removed to measure the magnetization decay. The results are shown in Fig. 8(b), where the continuous curve shows the excellent fit to the stretched exponent formula with $M_0 = 0.273$ μ_B/f.u., $M_r = 0.004$ μ_B/f.u., $\tau = (566 \pm 6)$ s, $\alpha = 0.603$ at 15 K, and $M_0 = 0.629$ μ_B/f.u., $M_r = 0.014$ μ_B/f.u., $\tau = (832 \pm 7)$ s, $\alpha = 0.546$ at 10 K. The values of the exponent α are in the span for spin glasses and cluster spin glasses, which suggests the strongly polydispersive relaxation nature of the glassy systems.

H. Electronic structure

To give firm footing to the interpretation of the magnetic properties of LSNMO, we have performed first-principles calculations to get quantitative insights into the microscopic origin of various magnetic interactions. The existence of ASD contributing to multiple AFM or FM transitions is also explored. We begin by investigating the ground-state properties of the ordered LNMO with 25% doping with an isoelectric Sm atom substituted at one of the La sites in the conventional unit
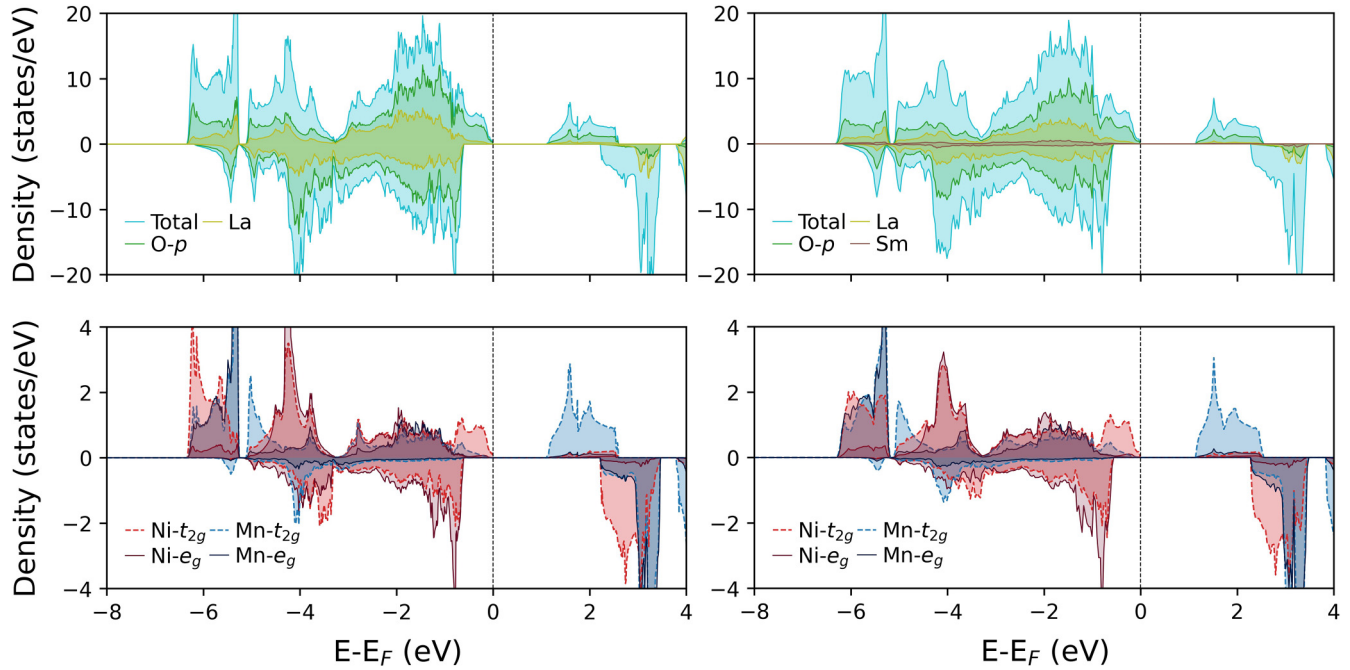
FIG. 9. Upper panel shows the spin-resolved total density of the pristine LNMO in the left column and LSNMO in the right column for the chemical ordered and ferromagnetic phase. It also shows the density projections on p orbital of oxygen atoms and La atoms in the right column; the left column also includes the contributions of the Sm atom. The bottom panels show the spin-polarized partial density of states for Ni-t_{2g}, Ni-e_g and Mn-t_{2g}, Mn-e_g, respectively. The Fermi level in the DOS is set to 0 eV.

cell of 20 atoms in the monoclinic phase. We relaxed the ionic positions at fixed experimental lattice constants described in Table I. The relaxed atomic positions and bond lengths have slight variations from the experimental data in the FM state (see Table I).

In FM configurations, each NiO$_6$ octahedra is tilted with respect to MnO$_6$ octahedra, giving rise to the Ni–O–Mn bond angles varying between 154.3° to 159.37°, depending on the position of the doped Sm atom. However, out of plane, the Ni–O$_3$-Mn bond angle changes significantly with a variation of 153° to 159°, whereas experimental results suggested it to be 173.55°. This is due to the position of the O atom; in particular, the O$_3$ oxygen atom differs noticeably from the experimental structure. This has already been reported in the literature [90,91]. Experimental structures may have antiphase disorders in the system, and the possibility of oxygen defects cannot be ignored either. This also gives a significant change in Ni–O$_3$ (2.03 Å) and Mn–O$_3$ (1.93 Å) bonds compared to the experimental values in Table I.

The ground-state magnetic configuration was determined by considering standard spin orientations on the Ni and Mn sites forming the FM, A-type antiferromagnetic (AFM-A), C-type antiferromagnetic (AFM-C), ferrimagnetic (FiM), and E-type antiferromagnetic (AFM-E). We also explored two configurations where two Ni and one Mn sites had a parallel spin, and the second Mn atom had an antiparallel spin and vice versa. This implies the total magnetic moments in the system depend on whether the Ni or Mn atom has an opposite spin. A description of these configurations can be found in Supplemental Material [73]. Our calculations suggest that the FM configuration is the most stable, as also

described in the experiment; the second most stable configuration is the AFM-A (83 meV/f.u. higher), followed by AFM-C (169 meV/f.u. higher) and FiM (246 meV/f.u. higher). The two configurations where only one element out of four magnetic elements has spin down are also higher (120 meV/f.u.) in energy. However, this is not enough to explain the coexistence of various magnetic phases in the system and needs further investigation, which will be discussed in detail below.

Figure 9 shows the spin-polarized DOS for the chemically ordered, lowest energy FM configuration for both the pristine LNMO and LSNMO. LNMO has an electronic gap of 1.13 eV in the majority spin channel and 2.83 eV in the minority spin channel, qualitatively matching with previous reports [90]. Doping with an isoelectric Sm^{3+} atom at one of the La^{3+} sites in the unit cell leads to small changes of the band gaps to 1.17 eV and 2.90 eV for the major and minor spin channels, respectively. The valence states are mostly dominated by the p-orbital contributions from the oxygen atom and d-orbital states of Mn(Ni) atoms. The octahedral environment of Mn and Ni atoms split the Mn-d and Ni-d manifolds into t_{2g}^3 and e_g^2 levels.

The site-projected, spin-polarized partial DOS shows that the valence states of Ni and Mn consist of ($t_{2g\uparrow}^3$, $t_{2g\downarrow}^3$, $e_{g\uparrow}^2$) and ($t_{2g\uparrow}^3$), where $\uparrow$ and $\downarrow$ signify the majority and minority spin states, respectively. The conduction band is formed by the $e_{g\uparrow}^2$ orbital of the Mn atom in the major spin channel and $t_{2g\downarrow}^3$, $e_{g\downarrow}^2$ of Mn atoms and $e_{g\downarrow}^2$ of Ni atoms in the minor spin channel. There is significant mixing of Mn-$t_{2g\uparrow}^3$ states and O-p states with Ni-$t_{2g\uparrow}^3$ and Ni-$e_{g\uparrow}^2$ bands in the major spin channel, whereas Ni-$t_{2g\uparrow}^3$ bands are located in between

dominant O-p states and the Fermi level. In the up-spin channel, the Mn-$t_{2g\uparrow}^3$ bands are filled and separated by a gap of ~ 1.13 eV from the empty Mn-e$_{g\uparrow}^2$ levels. In the down-spin channel, both Mn-t$_{2g\downarrow}^2$ and Mn-e$_{g\downarrow}^2$ bands are located above the Fermi level in the energy range of ~ 2.0 to 4.0 eV. This results in the oxidation state of Mn and Ni being Mn^{4+} and Ni^{2+}, respectively, which agrees with the previous results in the pristine system [90]. The calculated magnetic moment per formula unit in the FM configuration of LSNMO is 4.93 μ_B, which is close to previously reported experimental values for LNMO [20,29,90]. Spin moments of Ni and Mn are 1.59 μ_B and 3.29 μ_B; small magnetic moments are also associated with the oxygen atoms. The variation of magnetic moments is expected with varying U parameters; an increment in the U parameter tends to more localization that affects the magnetic moment. Both LNMO and LSNMO are insulators in FM ground states. The ferromagnetism in these systems is expected to be dominated by the superexchange interaction of the half-filled d orbital of one of the metal ions with the vacant d orbital of another metal ion through the p orbital of the oxygen atom. The occupation of the Ni-d states and Mn-d states leads to the conclusion of FM superexchange in Ni^{2+}–O^{2-}–Mn^{4+}, similar to the pristine LNMO.

We estimated the Bader charge around Mn$_1$ and Mn$_2$ atoms, which were found to be 1.72 e$^-$, and around Ni$_1$ and Ni$_2$ atoms, yielding 1.20 e$^-$ for the pristine LNMO. Conversely, in the doped LSNMO system, the charges on both Mn atoms were determined to be 1.70 e$^-$, and on both Ni atoms, 1.19 e$^-$. Mn$_1$, Mn$_2$, Ni$_1$, and Ni$_2$ are further described in the supporting information. However, it is important to note that the concept of the oxidation state employed here is somewhat formal [92]. Specifically, an analysis of charge ordering reveals that the actual change in charge on Mn or Ni atoms is considerably less than that required for Mn to be in a Mn^{4+} state and Ni to be in a Ni^{2+} state. The charge associated with the Mn and Ni transition metals is delocalized from the metal center, meaning that the Bader charge on metals can only offer a relative, rather than an absolute, measure of the metal charge state, such as Mn^{4+} or Ni^{2+}. This behavior is well documented in transition-metal oxides [93]. Therefore, a comprehensive understanding of charge ordering in these perovskites should be deduced from the partial density of states and magnetic moments on the ions, as elaborated earlier.

Further, we used different magnetic configurations to calculate the exchange constants up to the fifth-nearest-neighbor (NN) interaction for the ordered and the first-NN interaction for the disordered phase. We calculated the LSNMO in both ordered and disordered phases for various magnetic configurations, as described in Supplemental Material [73]. For the oxidation states, we derived this information from the magnetic moments approximately. A magnetic moment for Ni larger than 1.5 μ_B and closer to 2.0 μ_B is considered the Ni^{2+} state, while a magnetic moment closer to 1.0 and less than 1.5 μ_B is considered the Ni^{3+} state. Similarly, in the case of Mn, if the magnetic moment is closer to 2.9 to 3.0 μ_B, then Mn is in the Mn^{4+} state, and if the magnetic moment is somewhat larger or equal to 3.5 μ_B, then Mn is in the Mn^{3+} state. We employed this approximation and constructed our Heisenberg Hamiltonian to solve the magnetic exchange
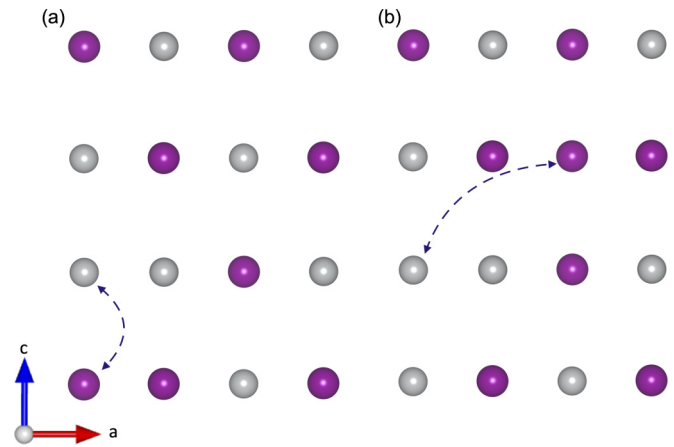

FIG. 10. Two-dimensional slice projection of $2\times1\times2$ supercell of LSNMO shows the antisite defect ordering. In the left panel (system A), the Ni and Mn sites are exchanged cooperatively, and in the right panel (system B), Ni and Mn sites are exchanged in different unit-cell positions. In both systems, there are four Mn and four Ni atoms occupying their correct sites, and the rest of the eight octahedral; sites are occupied by an equal number of Mn$_{Ni}$ (Mn atoms occupying Ni) or Ni$_{Mn}$ (Ni atom occupy Mn sites) antisites, resulting in 50% antisite mixing in the ordered phase. System A has a mutual exchange of Mn and Ni positions in one subunit, whereas in system B, Mn and Ni atoms are exchanged from two different subunits in the supercell.

coupling. We found that the NN interaction of Ni^{2+}–O^{2-}–Mn^{4+} superexchange is the most important with J$_0^{Mn^{4+}-Ni^{2+}} \approx$ 13.6 meV—the exchange constants for larger distance were at least two orders of magnitude lower. Assuming only NN interaction and using the total energies of the FM and AFM-A configuration results in $J_0^{Mn^{4+}-Ni^{2+}} \approx 13.9$ meV. This interaction between Mn^{4+} and Ni^{2+} is further increased in the disordered phases (see Supplemental Material [73]).

It has been well established that in LNMO, the SG behavior arises from the antisite and antiphase disorder in the system during the growth process [20,29]. In the experimental section, we also see similar behavior for LSNMO, but the transition temperatures are different from previously reported LNMO [20,29]. To test this in the notion of chemical disorder in LSNMO, we also investigated the antisite disorders in the unit cells and supercells. In the unit cell, we can exchange the position of one Ni and Mn atom and put the system in a disordered phase. In this phase, Mn octahedra corners are shared with two Mn and four Ni octahedra. Unlike the ordered phase, FiM (110 meV higher than FM) configurations in antisite phases have the second lowest energies after FM, whereas in the ordered phase it was AFM-A. However, in the experiments, it is highly unlikely to have perfect antisite phases. Rather, there will be combinations of some antisite phase boundaries in powder samples. To mimic the experiment and understand the properties of LSNMO in the presence of chemical disorder, we used $2\times1\times2$ supercells with eight f.u., which contains 80 atoms. One Ni–Mn combination is in the antisite phase, where Ni-Mn can exchange places mutually in nearest neighbors as described in Fig. 10(a) (denoted as system A in the following) or in different subunits as shown in Fig. 10(b) (system B). In both systems, there will be four

TABLE II. Comparison of energies in ASD phases in $2 \times 1 \times 2$ supercell for various magnetic configurations 1, 2, and 3 as described in the text. We described the correlated replacement of Ni and Mn atoms as system A and the uncorrelated replacement of Ni and Mn atoms as system B as described in the text. The energies are compared independently for system A and system B for both pristine LNMO and Sm-doped LNMO.

		LNMO			LSNMO		
		Energy (eV/f.u.)	Relative energy (eV/f.u.)	Magnetic moment (μ_B/f.u.)	Energy (eV/f.u.)	Relative energy (eV/f.u.)	Magnetic moment (μ_B/f.u.)
System A	Configuration 1	−73.857	0	4.942	−73.769	0	4.938
	Configuration 2	−73.632	0.225	1.467	−73.569	0.20	1.463
	Configuration 3	−73.783	0.075	3.478	−73.741	0.028	3.712
System B	Configuration 1	−73.832	0.025	4.941	−73.742	0.027	4.937
	Configuration 2	−73.617	0.240	1.457	−73.552	0.217	1.454
	Configuration 3	−73.757	0.100	3.474	−73.704	0.065	3.961

Mn and four Ni atoms occupying their correct sites. The rest of the eight (Mn, Ni) octahedral sites are occupied by an equal number of Mn_{Ni} (Mn atoms occupying Ni) or Ni_{Mn} (Ni atom occupy Mn sites) antisites. Five corners of Mn octahedra are shared with Ni and one corner is shared with Mn and vice versa. The average bond lengths in these antisite structures match better with experimental data in comparison to the ordered phase, which indicates the presence of ASD in the samples.

To understand the coupling between the magnetic moments of Mn and Ni cations in the presence of the ASD, we studied the energetic stability of three different magnetic configurations for both antisite structures in Fig. 10. We calculated three configurations: (1) FM phase in which all the spin directions are parallel both for Ni and Mn in the supercell (all the Mn and Ni ions have FM coupling); (2) FiM configuration, where all the Mn spins are antiparallel to the spins in the Ni atoms resulting in Mn ions having FM coupling with other Mn ions and AFM coupling with Ni ions and vice versa; and (3) Mn ions having AFM coupling with other Mn ions and FM coupling with Ni ions and vice versa, which results in three Ni and three Mn atoms in spin-up states and one Ni and one Mn atom in the supercell in the spin-down state. This last configuration is what we theoretically assume to have Ni^{2+}–O^{2-}–Mn^{4+} in FM exchange, Mn^{4+}–O^{2-}–Mn^{4+}, and Ni^{2+}–O^{2-}–Ni^{2+} in AFM exchange interactions. However, there is a strong possibility for other magnetic interactions such as Ni^{3+}–O^{2-}–Mn^{3+}, Ni^{3+}–O^{2-}–Ni^{2+}, Ni^{3+}–O^{2-}–Ni^{3+}, Ni^{2+}–O^{2-}–Ni^{2+}, Mn^{3+}–O^{2-}–Mn^{3+}, Mn^{4+}–O^{2-}–Mn^{4+}, and Mn^{3+}–O^{2-}–Mn^{4+} in these cases. These configurations for the two systems were relaxed for the ionic position at a fixed experimental lattice constant.

Table II shows the relative energies in three different magnetic phases for two antisite systems described in Fig. 10 for both the pristine system LNMO and Sm-doped system LSNMO. These disorders introduce some variations in the lengths of Mn–O and Ni–O bonds, respectively. There is a significant energy difference in these three configurations, clearly suggesting that configuration (3) is possible because they are only 75 meV and 100 meV higher than the FM phase in both antisite models. These energies are further reduced when the system is doped with Sm to 28 meV and 65 meV. In addition to this, configuration (1) has higher energies for

both systems as (0.20 eV higher for system A and 0.33 eV higher for system B) compared to FM configurations in the ordered LSNMO case. Overall, Sm atom doping does not change the structure significantly but reduces the energy differences between the most stable FM configuration in the ordered phase, and the difference between the most stable ASD configuration (1) and configuration (3). These suggest the mixed ordered and disordered phase in the powder sample results in various magnetic states found in the experiment and also possibly affects the transition temperature. In addition to relative energies in Table II, the total magnetic moment does not change significantly for LNMO and LSNMO. The magnetic moment for configuration (3) in the LSNMO case matches well with the observed saturation magnetization is 3.83 μ_B/f.u. in the inset of Fig. 3. The other two configurations have a magnetic moment 4.94 μ_B/f.u., 1.46 μ_B/f.u. for system A and 4.94 μ_B/f.u., 1.45 μ_B/f.u. for system B, respectively. Therefore, this qualitative picture suggests that the magnetic transitions at lower temperatures are the responses due to the ASD and APB in the LSNMO compound.

IV. CONCLUSIONS

In conclusion, we reported the synthesis of the LSNMO compound that crystallizes a monoclinic structure and exhibits the mixed valence states of Mn^{3+}/Mn^{4+} and Ni^{2+}/Ni^{3+} elements. The existence of mutually competing exchange interactions that are governed through mixed valence states of cations induces the magnetic frustration that originates various multiple magnetic transitions observed across $300 \rightarrow 5$ K. The presence of the inhomogeneous spin states and ASD in the LSNMO compound displays a low-temperature SG transition ($T_{SG} \sim 65 \pm 1$ K). The pinning of the moments across the FM and AFM in the inhomogeneous spin states results in the EB effect with $H_{EB} \sim 153$ Oe and $H_c \sim 1.2$ kOe under an applied field of 1 KOe. First-principles calculations also confirm that the LSNMO is an insulator, and various magnetic phases are the results of ASD in the sample. ASD gives the mixed exchange coupling between Mn and Ni atoms, which eventually results in a reduced magnetic moment. The observation of the EB effect and exceptional magnetic memory effect makes the LSNMO compound a potential candidate for understanding the spin-glass phase in magnetic frustrated systems.

[1] W. H. Meiklejohn and C. P. Bean, New magnetic anisotropy, Phys. Rev. **102**, 1413 (1956).

[2] H. Ohldag, A. Scholl, F. Nolting, E. Arenholz, S. Maat, A. T. Young, M. Carey, and J. Stöhr, Correlation between exchange bias and pinned interfacial spins, Phys. Rev. Lett. **91**, 017203 (2003).

[3] I. K. Schuller, R. Morales, X. Batlle, U. Nowak, and G. Güntherodt, Role of the antiferromagnetic bulk spins in exchange bias, J. Magn. Magn. Mater. **416**, 2 (2016).

[4] M. Kiwi, Exchange bias theory, J. Magn. Magn. Mater. **234**, 584 (2001).

[5] M. Ali, P. Adie, C. Marrows, D. Greig, B. Hickey, and R. Stamps, Exchange bias using a spin glass, Nat. Mater. **6**, 70 (2007).

[6] S. Giri, M. Patra, and S. Majumdar, Exchange bias effect in alloys and compounds, J. Phys.: Condens. Matter **23**, 073201 (2011).

[7] L. C. Barnsley, E. M. Gray, and C. J. Webb, Asymmetric reversal in aged high concentration CuMn alloy, J. Phys.: Condens. Matter **25**, 086003 (2013).

[8] K. H. Fischer and J. A. Hertz, *Spin Glasses*, Cambridge Studies in Magnetism (Cambridge University Press, 1991).

[9] K. Binder and A. P. Young, Spin glasses: Experimental facts, theoretical concepts, and open questions, Rev. Mod. Phys. **58**, 801 (1986).

[10] S. Nagata, P. H. Keesom, and H. R. Harrison, Low-dc-field susceptibility of CuMn spin glass, Phys. Rev. B **19**, 1633 (1979).

[11] D. K. Singh and Y. S. Lee, Nonconventional spin glass transition in a chemically ordered pyrochlore, Phys. Rev. Lett. **109**, 247201 (2012).

[12] P. Schiffer, A. P. Ramirez, D. A. Huse, P. L. Gammel, U. Yaron, D. J. Bishop, and A. J. Valentino, Frustration induced spin freezing in a site-ordered magnet: Gadolinium gallium garnet, Phys. Rev. Lett. **74**, 2379 (1995).

[13] J. M. De Teresa, M. R. Ibarra, J. García, J. Blasco, C. Ritter, P. A. Algarabel, C. Marquina, and A. del Moral, Spin-glass insulator state in $(Tb-La)_{2/3}Ca_{1/3}MnO_3$ perovskite, Phys. Rev. Lett. **76**, 3392 (1996).

[14] A. K. Kundu, P. Nordblad, and C. N. R. Rao, Nonequilibrium magnetic properties of single-crystalline $La_{0.7}Ca_{0.3}CoO_3$, Phys. Rev. B **72**, 144423 (2005).

[15] E. Maniv, R. A. Murphy, S. C. Haley, S. Doyle, C. John, A. Maniv, S. K. Ramakrishna, Y.-L. Tang, P. Ercius, R. Ramesh *et al.*, Exchange bias due to coupling between coexisting antiferromagnetic and spin-glass orders, Nat. Phys. **17**, 525 (2021).

[16] T. Murata, Y. Kozuka, M. Uchida, and M. Kawasaki, Magnetic properties of spin frustrated spinel $ZnFe_2O_4/ZnCr_2O_4$ superlattices, J. Appl. Phys. **118**, 193901 (2015).

[17] P. A. Kumar, R. Mathieu, P. Nordblad, S. Ray, O. Karis, G. Andersson, and D. D. Sarma, Reentrant superspin glass phase in a $La_{0.82}Ca_{0.18}MnO_3$ ferromagnetic insulator, Phys. Rev. X **4**, 011037 (2014).

[18] S. K. Mishra, F. Radu, H. A. Dürr, and W. Eberhardt, Training-induced positive exchange bias in NiFe/IrMn bilayers, Phys. Rev. Lett. **102**, 177208 (2009).

[19] J. A. Mydosh, *Spin Glasses: An Experimental Introduction* (CRC press, London, 1993).

[20] D. Choudhury, P. Mandal, R. Mathieu, A. Hazarika, S. Rajan, A. Sundaresan, U. V. Waghmare, R. Knut, O. Karis, P. Nordblad, and D. D. Sarma, Near-room-temperature colossal magnetodielectricity and multiglass properties in partially disordered La_2NiMnO_6, Phys. Rev. Lett. **108**, 127201 (2012).

[21] K. D. Chandrasekhar, A. K. Das, C. Mitra, and A. Venimadhav, The extrinsic origin of the magnetodielectric effect in the double perovskite La_2NiMnO_6, J. Phys.: Condens. Matter **24**, 495901 (2012).

[22] S. Baidya and T. Saha-Dasgupta, Electronic structure and phonons in La_2CoMnO_6: A ferromagnetic insulator driven by coulomb-assisted spin-orbit coupling, Phys. Rev. B **84**, 035131 (2011).

[23] S. K. Giri, R. C. Sahoo, P. Dasgupta, A. Poddar, and T. K. Nath, Giant spontaneous exchange bias effect in $Sm_{1.5}Ca_{0.5}CoMnO_6$ perovskite, J. Phys. D **49**, 165002 (2016).

[24] R. C. Sahoo, Y. Takeuchi, A. Ohtomo, and Z. Hossain, Exchange bias and spin glass states driven by antisite disorder in the double perovskite compound $LaSrCoFeO_6$, Phys. Rev. B **100**, 214436 (2019).

[25] R. I. Dass, J.-Q. Yan, and J. B. Goodenough, Oxygen stoichiometry, ferromagnetism, and transport properties of $La_{2-x}NiMnO_{6+\delta}$, Phys. Rev. B **68**, 064415 (2003).

[26] N. S. Rogado, J. Li, A. W. Sleight, and M. A. Subramanian, Magnetocapacitance and magnetoresistance near room temperature in a ferromagnetic semiconductor: La_2MnNiO_6, Adv. Mater. **17**, 2225 (2005).

[27] S. F. Matar, M. A. Subramanian, A. Villesuzanne, V. Eyert, and M.-H. Whangbo, First principles investigation of the electronic structure of La_2MnNiO_6: An insulating ferromagnet, J. Magn. Magn. Mater. **308**, 116 (2007).

[28] J.-S. Kang, G. Kim, H. J. Lee, S. Kolesnik, B. Dabrowski, H. Lee, J.-Y. Kim, J. Lee, B. Kim, and B. I. Min, Investigation of valence states and electronic structure of ferromagnetic double-perovskite La_2MnNiO_6 by using synchrotron radiation, J. Appl. Phys. **105**, 07D721 (2009).

[29] S. Pal, S. Govinda, M. Goyal, Sharada Mukherjee, B. Pal, R. Saha, A. Sundaresan, S. Jana, O. Karis, J. W. Freeland, and D. D. Sarma, Effect of anti-site disorder on magnetism in La_2NiMnO_6, Phys. Rev. B **97**, 165137 (2018).

[30] Y. Guo, L. Shi, S. Zhou, J. Zhao, C. Wang, W. jing Liu, and S. Wei, Tunable exchange bias effect in Sr-doped double perovskite La_2MnNiO_6, J. Phys. D **46**, 175302 (2013).

[31] J. K. Murthy, K. D. Chandrasekhar, H. C. Wu, H. D. Yang, J. Y. Lin, and A. Venimadhav, Antisite disorder driven spontaneous exchange bias effect in $La_{2-x}Sr_xCoMnO_6(0 \leqslant x \leqslant 1)$, J. Phys.: Condens. Matter **28**, 086003 (2016).

[32] J.-S. Kang, H. J. Lee, D. H. Kim, S. Kolesnik, B. Dabrowski, K. Świerczek, J. Lee, B. Kim, and B. I. Min, Valence and spin states, and the metal-insulator transition in ferromagnetic $La_{2-x}Sr_xNiMnO_6(x = 0, 0.2)$, Phys. Rev. B **80**, 045115 (2009).

[33] R. Hissariya, R. Sharma, and S. Mishra, Antisites disorder mediated magnetization relaxation and polydispersity in La_2NiMnO_6 crystallites, J. Phys. Chem. Solids **181**, 111549 (2023).

[34] K. Yoshimatsu, K. Nogami, K. Watarai, K. Horiba, H. Kumigashira, O. Sakata, T. Oshima, and A. Ohtomo, Synthesis and magnetic properties of double-perovskite oxide La_2MnFeO_6 thin films, Phys. Rev. B **91**, 054421 (2015).

[35] C. Meneghini, S. Ray, F. Liscio, F. Bardelli, S. Mobilio, and D. D. Sarma, Nature of "disorder" in the ordered double perovskite Sr_2FeMoO_6, Phys. Rev. Lett. **103**, 046403 (2009).

[36] V. Shabadi, M. Major, P. Komissinskiy, M. Vafaee, A. Radetinac, M. Baghaie Yazdi, W. Donner, and L. Alff, Origin of superstructures in (double) perovskite thin films, J. Appl. Phys. **116**, 114901 (2014).

[37] H. Z. Guo, J. Burgess, E. Ada, S. Street, A. Gupta, M. N. Iliev, A. J. Kellock, C. Magen, M. Varela, and S. J. Pennycook, Influence of defects on structural and magnetic properties of multifunctional La_2NiMnO_6 thin films, Phys. Rev. B **77**, 174423 (2008).

[38] X. Wang, Y. Sui, Y. Li, L. Li, X. Zhang, Y. Wang, Z. Liu, W. Su, and J. Tang, The influence of the antiferromagnetic boundary on the magnetic property of La_2NiMnO_6, Appl. Phys. Lett. **95**, 252502 (2009).

[39] A. Khan, S. Chatterjee, T. K. Nath, and A. Taraphder, Defect-induced modulation of magnetic, electronic, and optical properties of the double-perovskite oxide La_2CoMnO_6, Phys. Rev. B **104**, 035152 (2021).

[40] W. F. Espinosa-García and G. M. Dalpian, Influence of defects on antidoping behavior in $SmNiO_3$, Phys. Rev. B **104**, 205106 (2021).

[41] S. Smadici, P. Abbamonte, A. Bhattacharya, X. Zhai, B. Jiang, A. Rusydi, J. N. Eckstein, S. D. Bader, and J.-M. Zuo, Electronic reconstruction at $SrMnO_3$-$LaMnO_3$ superlattice interfaces, Phys. Rev. Lett. **99**, 196404 (2007).

[42] M. Kitamura, M. Kobayashi, E. Sakai, M. Minohara, R. Yukawa, D. Shiga, K. Amemiya, Y. Nonaka, G. Shibata, A. Fujimori, H. Fujioka, K. Horiba, and H. Kumigashira, Relationship between charge redistribution and ferromagnetism at the heterointerface between the perovskite oxides $LaNiO_3/LaMnO_3$, Phys. Rev. B **100**, 245132 (2019).

[43] M. Wang, T. Zhu, H. Bai, Z. Yin, H. Xu, W. Shi, Z. Li, J. Zheng, Y. Gan, Y. Chen, B. Shen, Y. Chen, Q. Zhang, F. Hu, and J.-R. Sun, Layered ferromagnetic structure caused by the proximity effect and interlayer charge transfer for $LaNiO_3/LaMnO_3$ superlattices, Nano Lett. **24**, 1122 (2024).

[44] Y. Bai, Y. Xia, H. Li, L. Han, Z. Wang, X. Wu, S. Lv, X. Liu, and J. Meng, A-site-doping enhanced b-site ordering and correlated magnetic property in $La_{2-x}Bi_xCoMnO_6$, J. Phys. Chem. C **116**, 16841 (2012).

[45] R. Hissariya, V. Sathe, and S. Mishra, Antisite disorder mediated exchange bias effect and spin-glass state in $La_{2-x}Sm_xNiMnO_6$, J. Magn. Magn. Mater. **578**, 170769 (2023).

[46] P. Hohenberg and W. Kohn, Inhomogeneous electron gas, Phys. Rev. **136**, B864 (1964).

[47] G. Kresse and J. Furthmüller, Efficient iterative schemes for ab initio total-energy calculations using a plane-wave basis set, Phys. Rev. B **54**, 11169 (1996).

[48] J. P. Perdew, K. Burke, and Y. Wang, Generalized gradient approximation for the exchange-correlation hole of a many-electron system, Phys. Rev. B **54**, 16533 (1996).

[49] C. M. Frostenson, E. J. Granhed, V. Shukla, P. A. Olsson, E. Schröder, and P. Hyldgaard, Hard and soft materials: Putting consistent van der Waals density functionals to work, Electron. Struct. **4**, 014001 (2022).

[50] P. Hyldgaard, Y. Jiao, and V. Shukla, Screening nature of the van der waals density functional method: A review and analysis of the many-body physics foundation, J. Phys.: Condens. Matter **32**, 393001 (2020).

[51] V. Eyert, VO_2: A novel view from band theory, Phys. Rev. Lett. **107**, 016401 (2011).

[52] V. Shukla, Y. Jiao, J.-H. Lee, E. Schröder, J. B. Neaton, and P. Hyldgaard, Accurate nonempirical range-separated hybrid van der waals density functional for complex molecular problems, solids, and surfaces, Phys. Rev. X **12**, 041003 (2022).

[53] V. Shukla, Y. Jiao, C. M. Frostenson, and P. Hyldgaard, vdW-DF-ahcx: a range-separated van der Waals density functional hybrid, J. Phys.: Condens. Matter **34**, 025902 (2022).

[54] A. V. Krukau, O. A. Vydrov, A. F. Izmaylov, and G. E. Scuseria, Influence of the exchange screening parameter on the performance of screened hybrid functionals, J. Chem. Phys. **125**, 224106 (2006).

[55] S. L. Dudarev, G. A. Botton, S. Y. Savrasov, C. J. Humphreys, and A. P. Sutton, Electron-energy-loss spectra and the structural stability of nickel oxide: An LSDA+U study, Phys. Rev. B **57**, 1505 (1998).

[56] S. Pal, S. Jana, S. Govinda, B. Pal, S. Mukherjee, S. Keshavarz, D. Thonig, Y. Kvashnin, M. Pereiro, R. Mathieu, P. Nordblad, J. W. Freeland, O. Eriksson, O. Karis, and D. D. Sarma, Peculiar magnetic states in the double perovskite Nd_2NiMnO_6, Phys. Rev. B **100**, 045122 (2019).

[57] I. L. M. Locht, Y. O. Kvashnin, D. C. M. Rodrigues, M. Pereiro, A. Bergman, L. Bergqvist, A. I. Lichtenstein, M. I. Katsnelson, A. Delin, A. B. Klautau, B. Johansson, I. Di Marco, and O. Eriksson, Standard model of the rare earths analyzed from the Hubbard I approximation, Phys. Rev. B **94**, 085137 (2016).

[58] H. J. Monkhorst and J. D. Pack, Special points for Brillouin-zone integrations, Phys. Rev. B **13**, 5188 (1976).

[59] W. Tang, E. Sanville, and G. Henkelman, A grid-based Bader analysis algorithm without lattice bias, J. Phys.: Condens. Matter **21**, 084204 (2009).

[60] M. Tovar, G. Alejandro, A. Butera, A. Caneiro, M. T. Causa, F. Prado, and R. D. Sánchez, ESR and magnetization in Jahn-Teller distorted $LaMnO_{3+\delta}$ correlation with crystal structure, Phys. Rev. B **60**, 10199 (1999).

[61] J. Zhang, H. Zheng, Y. Ren, and J. F. Mitchell, High-pressure floating-zone growth of perovskite nickelate $LaNiO_3$ single crystals, Cryst. Growth Des. **17**, 2730 (2017).

[62] S. Catalano, M. Gibert, V. Bisogni, O. E. Peil, F. He, R. Sutarto, M. Viret, P. Zubko, R. Scherwitzl, A. Georges, G. A.

Sawatzky, T. Schmitt, and J.-M. Triscone, Electronic transitions in strained SmNiO$_3$ thin films, APL Mater. **2**, 116110 (2014).

[63] R. Hissariya, S. Babu, S. Ram, and S. K. Mishra, Spin-up conversion, exchange-interactions, and tailored magnetic properties in core-shell La$_2$NiMnO$_6$ of small crystallites, Nanotechnology **32**, 435702 (2021).

[64] J. Mantilla, M. Morales, W. Venceslau, L. Corredor, P. Morais, F. F. Aragón, S. W. da Silva, and J. A. Coaquira, Field-driven spin reorientation in SmMnO$_3$ polycrystalline powders, J. Alloys Compd. **845**, 156327 (2020).

[65] F. Fabian, P. Pedra, J. Duque, C. Meneses *et al.*, Synthesis and characterization of La(Cr,Fe,Mn)O$_3$ nanoparticles obtained by co-precipitation method, J. Magn. Magn. Mater. **379**, 80 (2015).

[66] S. Majumder, M. Tripathi, H. E. Fischer, D. O. de Souza, L. Olivi, A. K. Sinha, R. J. Choudhary, and D. M. Phase, Microscopic insights of magnetism in Sm$_2$NiMnO$_6$ double perovskite, Phys. Rev. B **105**, 094425 (2022).

[67] N. Yamazoe, Y. Teraoka, and T. Seiyama, TPD and XPS study on thermal behavior of absorbed oxygen in La$_{1-x}$Sr$_x$CoO$_3$, Chem. Lett. **10**, 1767 (1981).

[68] K. Tabata, I. Matsumoto, and S. Kohiki, Surface characterization and catalytic properties of La$_{1-x}$Sr$_x$CoO$_3$, J. Mater. Sci. **22**, 1882 (1987).

[69] L. G. Tejuca, J. L. G. Fierro, and J. M. Tascón, Structure and reactivity of perovskite-type oxides (Academic Press, 1989), pp. 237–328.

[70] L. Richter, S. D. Bader, and M. B. Brodsky, Ultraviolet, x-ray-photoelectron, and electron-energy-loss spectroscopy studies of LaCO$_3$ and oxygen chemisorbed on LaCO$_3$, Phys. Rev. B **22**, 3059 (1980).

[71] J. C. Dupin, D. Gonbeau, P. Vinatier, and A. Levasseur, Systematic XPS studies of metal oxides, hydroxides and peroxides, Phys. Chem. Chem. Phys. **2**, 1319 (2000).

[72] Z. An, Y. Zhuo, C. Xu, and C. Chen, Influence of the TiO$_2$ crystalline phase of MnO$_x$-TiO$_2$ catalysts for no oxidation, Chin. J. Catal. **35**, 120 (2014).

[73] See Supplemental Material at http://link.aps.org/supplemental/10.1103/PhysRevMaterials.8.074403 for valence state determination.

[74] X. Luo, B. Wang, Y. P. Sun, X. B. Zhu, and W. H. Song, Critical behavior of double perovskite La$_2$NiMnO$_6$, J. Phys.: Condens. Matter **20**, 465211 (2008).

[75] M. Nasir, A. K. Pathak, J. Kubik, D. Malaviya, V. Krupa, A. Dasgupta, and S. Sen, Enhanced B-site cation ordering and improved magnetic properties: Role of A-site Bi substitution in La$_2$NiMnO$_6$ double perovskites, J. Alloys Compd. **896**, 162713 (2022).

[76] Y. Li, Q. Lv, S. Feng, K. M. Ur Rehman, X. Kan, and X. Liu, A comparative investigation of B-site ordering and structure, magnetic, magnetocaloric effect, critical behavior in double perovskite Nd$_2$BMnO$_6$ (B = Co and Ni), Ceram. Int. **47**, 32599 (2021).

[77] H. Guo, A. Gupta, M. Varela, S. Pennycook, and J. Zhang, Local valence and magnetic characteristics of La$_2$NiMnO$_6$, Phys. Rev. B **79**, 172402 (2009).

[78] V. M. Gaikwad, K. K. Yadav, Sunaina, S. Chakraverty, S. Lofland, K. V. Ramanujachary, S. Nishanthi, A. K. Ganguli,

and M. Jha, Design of process for stabilization of La$_2$NiMnO$_6$ nanorods and their magnetic properties, J. Magn. Magn. Mater. **492**, 165652 (2019).

[79] R. R. Das, P. Parida, A. K. Bera, T. Chatterji, B. R. K. Nanda, and P. N. Santhosh, Giant exchange bias in the single-layered Ruddlesden-Popper perovskite SrLaCo$_{0.5}$Mn$_{0.5}$O$_4$, Phys. Rev. B **98**, 184417 (2018).

[80] M. Patra, M. Thakur, K. De, S. Majumdar, and S. Giri, Reply to "Comment on 'Particle size dependent exchange bias and cluster-glass states in LaMn$_{0.7}$Fe$_{0.3}$O$_3$,'" J. Phys.: Condens. Matter **21**, 078002 (2009).

[81] C. Binek, Training of the exchange-bias effect: A simple analytic approach, Phys. Rev. B **70**, 014421 (2004).

[82] H. Ahmadvand, H. Salamati, P. Kameli, A. Poddar, M. Acet, and K. Zakeri, Exchange bias in LaFeO$_3$ nanoparticles, J. Phys. D **43**, 245002 (2010).

[83] F. Radu and H. Zabel, Exchange bias effect of ferro-/antiferromagnetic heterostructures, in *Magnetic Heterostructures: Advances and Perspectives in Spinstructures and Spintransport*, edited by H. Zabel and S. D. Bader (Springer, Berlin, 2008), pp. 97–184.

[84] D. Paccard, C. Schlenker, O. Massenet, R. Montmory, and A. Yelon, A new property of ferromagnetic-antiferromagnetic coupling, Phys. Status Solidi B **16**, 301 (1966).

[85] M. Giot, A. Pautrat, G. André, D. Saurel, M. Hervieu, and J. Rodriguez-Carvajal, Magnetic states and spin-glass properties in Bi$_{0.67}$Ca$_{0.33}$MnO$_3$: Macroscopic ac measurements and neutron scattering, Phys. Rev. B **77**, 134445 (2008).

[86] J.-Y. Ji, P.-H. Shih, T.-S. Chan, Y.-R. Ma, and S. Y. Wu, Magnetic properties of cluster glassy Ni/NiO core-shell nanoparticles: An investigation of their static and dynamic magnetization, Nanoscale Res. Lett. **10**, 243 (2015).

[87] A. C. Gandhi, R. Selvam, C.-L. Cheng, and S. Y. Wu, Room temperature magnetic memory effect in nanodiamond/γ-Fe$_2$O$_3$ composites, Nanomaterials **11**, 648 (2021).

[88] Z. Tian, L. Xu, Y. Gao, S. Yuan, and Z. Xia, Magnetic memory effect at room temperature in exchange coupled NiFe$_2$O$_4$-NiO nanogranular system, Appl. Phys. Lett. **111**, 182406 (2017).

[89] P. K. Pandey, R. J. Choudhary, and D. M. Phase, Magnetic behavior of layered perovskite Sr$_2$CoO$_4$ thin film, Appl. Phys. Lett. **103**, 132413 (2013).

[90] H. Das, U. V. Waghmare, T. Saha-Dasgupta, and D. D. Sarma, Electronic structure, phonons, and dielectric anomaly in ferromagnetic insulating double pervoskite La$_2$NiMnO$_6$, Phys. Rev. Lett. **100**, 186402 (2008).

[91] C. L. Bull, D. Gleeson, and K. S. Knight, Determination of B-site ordering and structural transformations in the mixed transition metal perovskites La$_2$CoMnO$_6$ and La$_2$NiMnO$_6$, J. Phys.: Condens. Matter **15**, 4927 (2003).

[92] A. Boev, S. Fedotov, A. Abakumov, K. Stevenson, G. Henkelman, and D. Aksyonov, The role of antisite defect pairs in surface reconstruction of layered AMO$_2$ oxides: A DFT+U study, Appl. Surf. Sci. **537**, 147750 (2021).

[93] M. K. Aydinol, A. F. Kohan, G. Ceder, K. Cho, and J. Joannopoulos, Ab initio study of lithium intercalation in metal oxides and metal dichalcogenides, Phys. Rev. B **56**, 1354 (1997).